Conceptual-based design of an ultrabroadband microwave metamaterial absorber

Sichao Qu[a,1], Yuxiao Hou[a,1], and Ping Sheng[a,2]

[a]Department of Physics, Hong Kong University of Science and Technology, Hong Kong, China

Edited by David A. Weitz, Harvard University, Cambridge, MA, and approved August 4, 2021 (received for review June 07, 2021)

By introducing metallic ring structural dipole resonances in the microwave regime, we have designed and realized a metamaterial absorber with hierarchical structures that can display an averaged −19.4 dB reflection loss (~99% absorption) from 3 to 40 GHz. The measured performance is independent of the polarizations of the incident wave at normal incidence, while absorption at oblique incidence remains considerably effective up to 45°. We provide a conceptual basis for our absorber design based on the capacitive-coupled electrical dipole resonances in the lateral plane, coupled to the standing wave along the incident wave direction. To realize broadband impedance matching, resistive dissipation of the metallic ring is optimally tuned by using the approach of dispersion engineering. To further extend the absorption spectrum to an ultrabroadband range, we employ a double-layer self-similar structure in conjunction with the absorption of the diffracted waves at the higher end of the frequency spectrum. The overall thickness of the final sample is 14.2 mm, only 5% over the theoretical minimum thickness dictated by the causality limit.

metamaterials | microwave absorption | high-impedance resonances | dipole resonances | hierarchical structures

The advent of fifth generation (5G) technology implies an order of magnitude, or more, microwave power permeating the 5G-active space, owing to the usage of multiple high-frequency microwave bands (1), a significant increase in transmission stations, and the fact that the microwave power varies quadratically as a function of frequency. Associated with this microwave power increase, there is a need for balancing the necessary monitoring activities and privacy as well as for remediating health concerns (2–4) arising from the long-term exposure to a much higher microwave power environment. A suitable microwave absorption structure can play an important role in resolving such issues. Meanwhile, there also exists extensive demands for electromagnetic absorption, with applications in electromagnetic compatibility (5), radar cross-section reduction (6), energy harvesting (7), etc. The recent development of metamaterial absorbers, based on designed structures with subwavelength thickness, has injected new momentum to this subject, with potential applications (8) to broad frequency bands ranging from microwave to terahertz (9–11), infrared (12–14), and visible light (15, 16). Due to microwave's long wavelength and high penetrability through solids, its absorption has always been the most challenging.

An ideal microwave absorber should absorb over a wide frequency bandwidth, with simple geometry for both experimental implementation and mass production. However, recent metamaterial-based absorbers can only display near-perfect absorption at either one frequency (13, 17–19) or several discretized frequencies (9, 20) due to the inherent resonance-based mechanism of metamaterials and their attendant dispersive characteristics (21). In order to extend the absorption frequency spectrum, many efforts have been devoted to either increasing the dissipation (22–26), for example, by using resistive sheets or loading with lumped elements, or superposing resonant units (27–31), for example, by exploiting multilayer patch absorbers. Yet, the broadband performance has still been limited, and the geometry of such structures has evolved toward ever-more complexity and sophistication.

In this work, the basic building block in our design is just a metallic ring that is fabricated by the printed circuit board (PCB) technology. The final integrated sample can exhibit near-perfect absorption from 3 to 40 GHz, covering the whole high-frequency 5G bands (32). Another crucial measure of an absorber is its thickness. While a thick enough absorber can absorb everything over all frequency regimes, it is nevertheless impractical in terms of applications. For a passive absorber, there is a common standard set by the causality-dictated minimum sample thickness that is associated with any given reflection spectrum (33). In our case, the overall thickness of the absorber is 14.2 mm, only 5% over the minimum thickness dictated by the causality limit. This theoretical limit also plays a crucial role in the impedance design of the acoustic (34–38) and microwave transmission line network systems (6, 39, 40). The causal optimality of broadband metamaterial absorber has been reported in acoustic systems (35, 36). However, to the best of our knowledge, the electromagnetic counterpart has not yet been experimentally realized, which therefore serves as one of our motivating targets. Although metallic ring structures have been extensively studied in the literature (8, 21, 41, 42), it has not been found that they can serve as the basis for broadband microwave absorption. We show that the crucial underlying physics lies in the generation of two high-impedance resonances from the interaction of the electric dipole resonance of the metallic ring with its image resonance, and the resulting impedance matching attained by adding resistive loss to the metallic ring. The latter is usually denoted dispersion engineering (21).

Here, we iterate the following four conceptual-based elements that underpin our absorber design and its excellent performance.

Significance

While microwave absorption is a widely pursued topic, a conceptual-based design can offer a theoretical basis for generalization and improvements. We offer a design recipe for ultrabroadband absorption based on the use of electrical dipole resonance in a metallic ring to generate, via interaction with its image resonance, two high-impedance resonances. Impedance matching over the frequency range in between the two resonances is obtained by adding resistance to the metallic ring. To extend the absorption to an ultrabroadband spectrum, we employ a double-layer self-similar structure in conjunction with absorption of the diffracted waves at the higher frequency end. The resulting absorber pushes the overall performance close to the causality limit over a large absorption bandwidth.

Author contributions: P.S. designed research; S.Q., Y.H., and P.S. performed research; S.Q., Y.H., and P.S. analyzed data; and S.Q. and P.S. wrote the paper.

The authors declare no competing interest.

This article is a PNAS Direct Submission.

[1]S.Q. and Y.H. contributed equally to this work.

[2]To whom correspondence may be addressed. Email: sheng@ust.hk.

This article contains supporting information online at https://www.pnas.org/lookup/suppl/doi:10.1073/pnas.2110490118/-/DCSupplemental.

Published September 3, 2021.

First is the use of electrical dipole resonance and the interaction with its image that insures an appreciable magnetic permeability with the generation of two high-impedance resonances in the microwave regime. Second is the use of dispersion engineering via the tuning of the dissipative resistance to achieve broadband impedance matching. Third is the use of self-similar hierarchical structure to extend the absorption spectrum to the ultrabroadband regime. Fourth is the absorption of the diffraction orders in the higher frequency regime by using foam patches. Below, we detail each of the conceptual elements together with their structural realizations.

Results

Metallic Ring. The basic element of our absorber is a rectangular metallic ring, each separated from its neighbor by a capacitive gap (Fig. 1*A*, two of the half rings are plotted to show the periodic configuration). The rings are embedded on PCB stipes [FR4 with relative permittivity $\epsilon_1 = 4.3(1 + 0.025i)$], which are structured to form a two-dimensional checkerboard array (Fig. 1*B*) to attain polarization-independent properties. The lattice constant (i.e., lateral spatial periodicity) is $a_1 = 24$ mm. Detailed geometry information is available in *SI Appendix*, *Sample geometry*.

Capacitively-Coupled Electrical Dipole Resonance. A metallic ring can be regarded as two metallic segments fused together on their two ends. If the length of each metallic segment corresponds to half wavelength of the incident wave, an electrical dipole resonance can be excited. The occurrence of this resonance may be further enhanced through capacitive coupling between the neighboring rings (Fig. 1*A*). To investigate this dipole resonance through simulations, we apply the periodic boundary condition around the unit cell (indicated by the black frame in Fig. 1*B*), with an incident plane wave from the top side. The excited dipole mode would radiate upward and downward, and the resulting fields in steady state can be divided into the incident field plus the scattered radiating field. In particular, the energy ratios can be extracted from the S parameters, that is, reflection $R = |S_{11}|^2$, transmission $T = |S_{21}|^2$, and the absorption $A = 1 - R - T$. It is shown in Fig. 1*C* that a resonance is located at 6.25 GHz for our rectangular metallic ring (with width $w_1 = 16$ mm and height $h_1 = 8.3$ mm), characterized by the minimal transmission and a maximum in reflection. To verify our understanding that this is indeed a half wavelength electrical dipole resonance, we deviate the width of the ring from its original value $w_1 = 16$ mm and compare the predicted frequency $f_d = c/\lambda = c/[2(w_1+h_1)]$ with the resonance peaks given by the simulations. Good agreements are obtained as seen in Fig. 1*D*. We note that the resonance also occurs with enhanced electric field in the gap between two nearby rings, which means that the resonance is of a collective response. The fact that it is an electric dipole resonance can be further confirmed by the symmetrical radiating electric field pattern and the anti-symmetrical magnetic field pattern (Fig. 1 *E* and *F*). Owing to the scattered radiation, the width of the resonance peak is noted to be fairly broad.

Interaction with the Image Mode and the High-Impedance Resonances. In Fig. 2*A*, we show the effect of introducing a metallic boundary at the bottom side of the sample. By approximating the metallic boundary as a perfect electric conductor (PEC) plane, its effect can be determined through the interaction of the current loop with its image. At specified frequencies, the retardation effect can lead to high-impedance resonances as detailed below. Consider the current densities J_1 and J_2 in Fig. 2*A*, equally distant from the PEC plane with a separation $d = 14.2$ mm. Under the Lorentz gauge (43), the current density is the source term of the wave equation for the vector potential A. In Fig. 2*A*, J_1 is positive (to the right); it emits a signal that travels with the speed of light toward J_2. Provided the distance between J_1 and J_2—$2d$ in the present case—corresponds to a phase difference of π, then when the signal reaches J_2, it would have acquired an opposite sign. However, since J_2 is along the negative direction, the arrival signal is exactly in phase with the signal emitted by J_2, leading to an enhancement. The enhanced signal would travel back to J_1 with a phase change of π again and encounters an in phase–emitted signal from J_1, and in this manner, the wave amplitude is reinforced back and forth, leading to a longitudinal resonant behavior. Since the electric field corresponds with the time derivative of A, one can expect a maximum of the electric field to occur at the J_1 plane, implying a perfect magnetic conductor (PMC) condition, that is, a high-impedance resonance. Indeed, through simulations, it was found that at 3.38 and 8.02 GHz, the upper surface of the ring structure, that is, the J_1 plane, is indeed an antinode of the electric field, which can be recognized as the artificial PMC effect induced by a magnetic resonance (44–46). Between the two high-impedance magnetic resonances, there exists a magnetic antiresonance with zero impedance at 5.32 GHz, at which the retardation effect leads

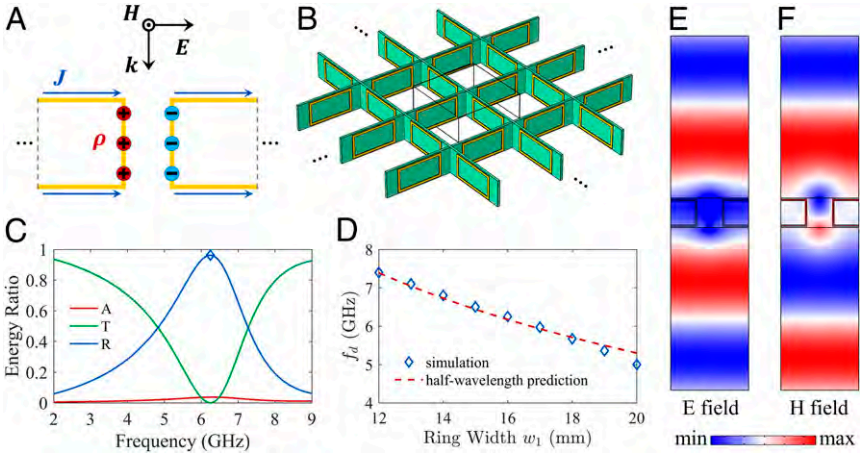

Fig. 1. (*A*) The geometry of the metallic ring structure (yellow) and its capacitive gap, serving as the basis for a resonant electrical dipole. Here, only half of the ring is drawn, and the dashed lines imply the periodic conditions. The arrows and circles illustrate the current density and charge density, respectively. (*B*) The periodic two-dimensional array constructed by the ring structures embedded in the PCB substrates (green plates). The black box denotes one unit cell. (*C*) Energy ratios of the absorption A, transmission T, and reflection R. (*D*) A comparison between the simulation results and the half wavelength prediction. The resonant frequencies are plotted as a function of varying the lateral width of the ring. (*E* and *F*) The scattered radiating electric field and magnetic field at the 6.25 GHz resonance.

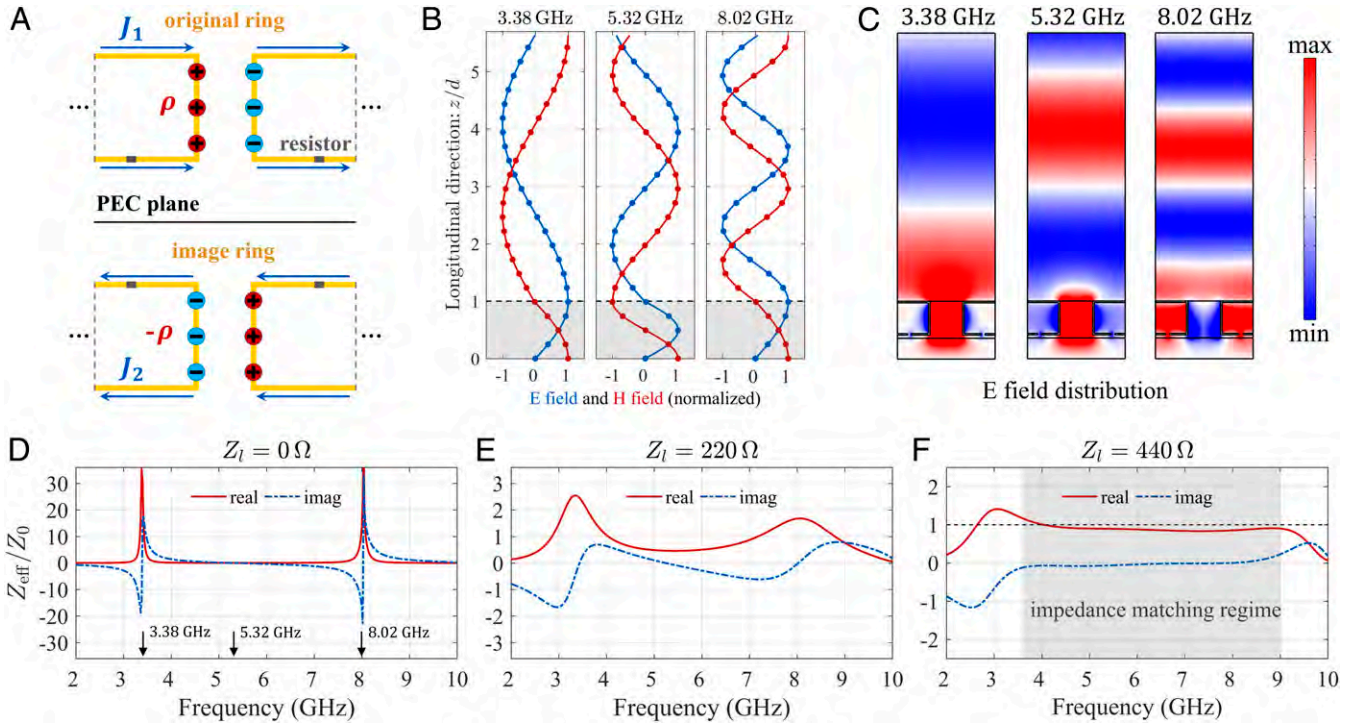

Fig. 2. (*A*) Schematics of the original ring and its mirror image with the presence of the PEC plane. The rings are loaded with two tunable resistors (gray patches). (*B*) The simulated standing wave patterns for effective medium with n_{eff}, indicated by gray regions. The blue and red curves denote the E field and H field respectively, with its amplitude normalized to be unity. (*C*) The simulated standing electric fields for the real ring structure excited by an incident plane wave from the top side. At 3.38 and 8.02 GHz, the upper surface of the ring exhibits antinodes of the E field (PMC effect), while at 5.32 GHz, it is a node for the E field (PEC effect). (*D–F*) The comparison of the effective normalized impedance with the loaded resistance of 0, 220, and 440 Ω, respectively. The shadowed gray region in *F* highlights the impedance matching regime from 3.6 to 9 GHz.

to a phase change of 2π between J_1 and J_2. It should be noted that the magnetic antiresonance is the electric resonance, and vice versa (13, 28), due to the distinct symmetries of the resonant modes. Similar correspondences were also reported in acoustic systems (47–49).

We can replace the metallic ring structure by an effective medium with an effective refraction index n_{eff} (see gray regions in Fig. 2*B*). It turns out that by setting $n_{eff} = 1.6$, 2.0, and 0.66 for 3.38, 5.32, and 8.02 GHz, respectively, the resulting far fields (Fig. 2*B*) can be fitted to be identical with those shown in Fig. 2*C*. The same PMC effects are also seen at the upper plane of effective medium, characterized by the electric field antinode and magnetic field node (Fig. 2*B*). Inside the effective medium, the fields undergo a phase shift of $\pi/2$, π, and $\pi/2$ for 3.38, 5.32, and 8.02 GHz, respectively. The only "surprise" here is that the phase shift at 8.02 GHz is only $\pi/2$ instead of the intuitively expected $3\pi/2$. This is because the metallic ring structure prevents the electric field from having a node inside the ring as one can see in the 8.02 GHz subplots of Fig. 2*C*. It should be noted that similar considerations leading to a resonance behavior can be applied to the current component in Fig. 2*A* close to the PEC plane in conjunction with the interaction with its image. That turns out to be unnecessary because the small distance of separation between the current (close to the PEC plane) and its image implies a much higher resonance frequency in which the diffraction effect appears and therefore the underlying physical picture of our description above is no longer valid.

Dispersion Engineering for Broadband Impedance Matching. The resonant behaviors can be quantitatively reflected in the effective impedance $Z_{eff}(\omega)$. Details of the extraction method (28, 50) for the effective parameters are available in *SI Appendix*, *Extraction method for the effective parameters*. For a small loaded resistance ($Z_l \to 0\,\Omega$), the effective impedance can be written in Lorentz forms (28, 47):

$$Z_{eff}(\omega) = \sum_i \frac{-i\omega\alpha_i}{\omega_i^2 - \omega^2 - i\beta_i\omega}, \quad [1]$$

where ω_i is the ith resonant frequency, α_i is its oscillation strength, and β_i denotes its dissipation coefficient. In Fig. 2*D*, we show that at 3.38 and 8.02 GHz, the real part of Z_{eff} exhibits high peaks, while at 5.32 GHz, the impedance is the zero (magnetic antiresonance). Since the impedance matching condition requires $Z_{eff} \cong Z_0$ (see more details on theoretical requirements for near-perfect absorption in *SI Appendix*, *Theoretical requirements for near-perfect absorption*), we would like to spread the high impedance of the two magnetic resonances evenly over the frequency range in between the two resonances. This can be achieved by fixing two chip resistors symmetrically at the bottom of the ring (see gray patches in Fig. 2*A*). By adjusting the load resistance Z_l, it can be seen from Fig. 2 *D–F* that at an optimal value of $Z_l = 440\,\Omega$, the real part of Z_{eff} is almost matched to Z_0, while the imaginary part is close to zero (see the gray highlighted regime from 3.6 to 9.0 GHz in Fig. 2*F*). In this manner, we have shown that the metallic ring structure, together with the PEC backing, can exhibit excellent absorption from 3.6 to 9 GHz with more than −20 dB reflection loss (Fig. 3*A*). It should be noted that the dispersion engineering for impedance matching can only be effective over a limited frequency range. This is due to the fact that over all frequencies, the causality-governed Kramer–Kronig relations (43) must hold.

Self-Similar Hierarchical Structures. The physical phenomena of waves are closely linked to the ratio between the wavelength and the size of the structure, usually denoted the scaling factor (34).

For instance, if the dimensions of the ring structure are uniformly scaled by α (<1), while the material properties (e.g., the resistance, dielectric constant of the substrate) are kept unchanged, the operating band can be extended to a higher frequency range, that is, from 3.6/α-9/α GHz. In our case, the optimal value of α is chosen to be 1/4 simply because the other values cannot cover either the high-frequency or the low-frequency end of the absorption spectrum as well as 1/4. Details on the scaling factor determination is given in *SI Appendix*, *Scaling factor determination*. In actual implementation of the scaled structures, not every material property can be kept the same under realistic considerations [e.g., the dielectric constant of the high-frequency PCB substrate is usually smaller in the industrial production, which is Rogers 5880 with relative permittivity $\epsilon_2 = 2.2(1 + 0.0009i)$ in our case]. Therefore, the geometric parameters for the smaller ring structure have to be slightly adjusted to retain the scaling property of the operating frequency band by a repeat application of dispersion engineering. However, the loaded resistance (Z_l = 440 Ω) remains unchanged, and the lattice constant is strictly scaled by the 1/4 factor (i.e., $a_2 = a_1/4$). Geometry information for optimized smaller ring structures is also available in *SI Appendix*, *Sample geometry*. In this way, it turns out that the reflection loss of smaller ring structures is close to −20 dB from 10 to 36 GHz (Fig. 3*B*).

Splicing the Reflection Loss Spectra. The ultimate purpose of designing two similarly structured arrays with scaled spatial dimensions is to splice the absorption spectra to attain the ultrabroadband regime. Remarkably, the integrated hierarchical structure (see Fig. 3 *C*, *Inset* for the schematic of the unit cell and Fig. 3*D* for a photo of fabricated sample) exhibits spliced ultrabroadband reflection loss spectrum from 3 to 35 GHz (see the blue circles in Fig. 3*C*). Good agreements are witnessed between the simulation and experimental results. Note that the overall thickness is the summation of the height of the first layer l_1 and second layer l_2 (i.e., $d = l_1 + l_2$ = 14.2 mm). However, diffraction invariably arises in the higher frequency range over such an ultrabroadband coverage. A generalized definition of "absorption" is needed by including diffraction into consideration (25) because our absorber works beyond the subwavelength regime, that is, $f > c/a_1 = 12.5$ GHz. In the absence of transmission, reflection loss in the linear scale is defined by $1 - R$, which is actually the summation of diffraction and absorption (i.e., $1 - R = D + A$). Here, the energy ratios can be expressed by the S parameters: $R = |S_{11}|^2$, $D = \sum_{i>1}|S_{i1}|^2$. In logarithmic dB scale, reflection loss is defined by the value of 10 $\log_{10}(R)$ in accordance with the textbook definition in microwave engineering (6).

Ultrabroadband Reflection Loss. We interpret the reflection loss mechanisms of the integrated hierarchical structure as follows. Absorption in the lower frequency range (by the upper layer) is minimally affected by the lower layer, owing to the smaller dimensions of the rings as compared to the relevant wavelength. The individual layer's absorption mechanism has been guaranteed by impedance matching as described in Fig. 2 *D*–*F*. In the higher frequency regime, however, the upper layer would diffract a part of the incident wave, while the lower layer would absorb the remaining part. In order to dissipate the diffracted components, we use the microwave-absorbing foam patches (Dalian Dongxin FCT40) to fill the upper layer interstitial spaces of the checkerboard array without increasing the overall thickness (Fig. 3*E*). The foam patches (with a thickness of 9 mm) are chosen to be porous and dissipative with low mass density and small loss angle (see details on the simulation modeling of the foam in *SI Appendix*, *Modeling the foam by using the Debye model*). In this way, the reflection loss spectrum is extended to 40 GHz (see the orange circles in Fig. 3*C*) with a large fraction of the diffraction effectively absorbed inside the sample, which can be verified through simulations (see the calculation of diffraction orders in *SI Appendix*, *Diffraction orders and their absorption*). In fact, we believe that with the foam patches, the sample can exhibit excellent absorption at frequencies much higher than 40 GHz, which is the limit of our measurement system.

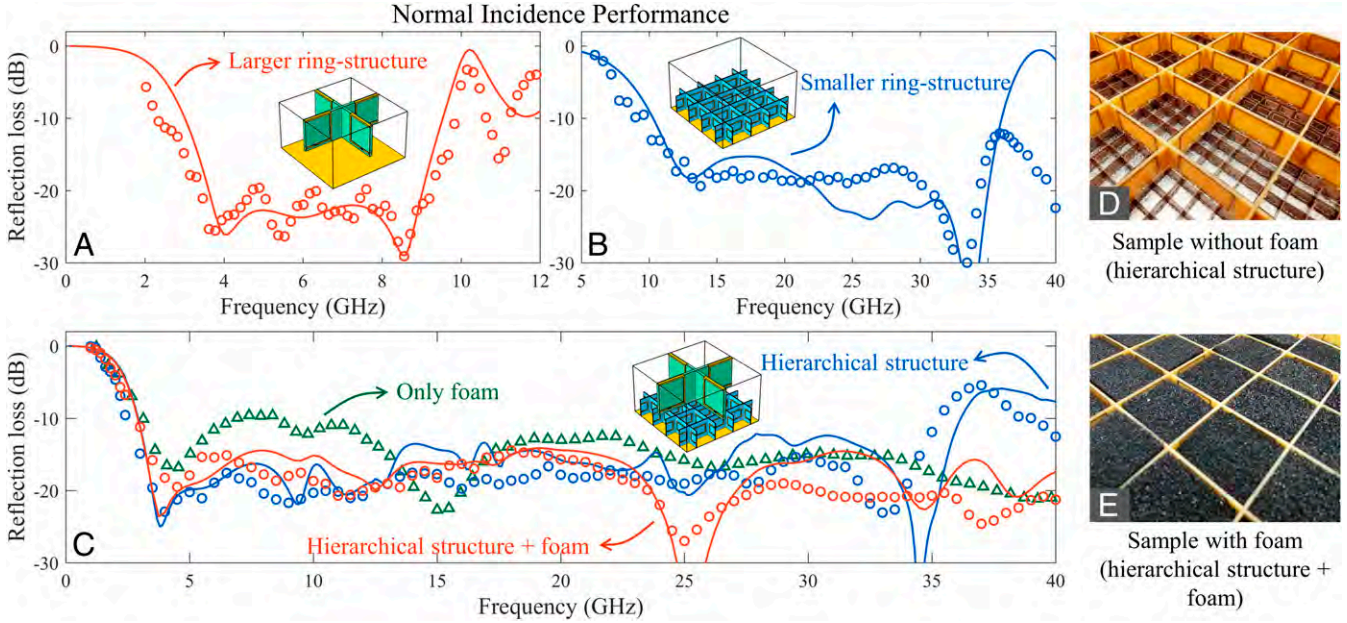

Fig. 3. Normal incidence performance. (*A* and *B*) The reflection loss spectra (in dB scale) of the individual larger-ring structure and the smaller ring structure, respectively. (*C*) The spliced reflection loss spectra (in dB scale) of the hierarchical structures with and without the foam patches together with the same results for the foam with identical thickness as the sample. The solid lines denote the simulation results with the unit cells shown in *Insets* in each figure, and the circles/triangles are the measured results. (*D*) A photo of the fabricated sample assembled into two-dimensional arrays with hierarchical structures. (*E*) The same for the structure with foam patches filled in the interstitial space.

Performance Evaluation and Comparison. We introduce two quantitative indicators to evaluate the measured performance as well as to facilitate the comparison with published prior results. The first indicator is the causality ratio defined by $R_c = d/d_{\min}$ in which the actual thickness of our absorber $d = 14.2$ mm, and the causality-dictated minimum thickness (33, 36) is given by

$$d_{\min} = \frac{1}{4\pi^2}\frac{\mu_0}{\mu_{\text{eff}}}\left|\int_0^\infty \ln(R(\lambda))\right| d\lambda, \qquad [2]$$

where $R(\lambda)$ is the reflected energy as a function of the wavelength λ, and $\mu_0/\mu_{\text{eff}} \cong 1$ for nonmagnetic absorbers, which is the case considered in this work. By inserting the measured reflection spectrum (orange circles in Fig. 3*C*) of the hierarchical structures with foam patches into Eq. **2**, we obtain $d_{\min} = 13.5$ mm and $R_c = 1.05$, which means that our absorber closely approaches the causality limit. The causality ratio R_c for the hierarchical structure without the foam patches (Fig. 3*D*) does not deviate from 1.05 too much since the higher frequency part has negligible contribution to the integral of Eq. **2**. The second indicator is the relative bandwidth, defined by

$$B_w = 2(f_2 - f_1)/(f_2 + f_1), \qquad [3]$$

where f_1 and f_2 denote the minimum and maximum frequencies corresponding to the operating band for at least −10 dB reflection loss (25). In our case, $f_1 = 3$ GHz and $f_2 = 40$ GHz, so $B_w = 1.72$. It should be noted that if $f_2/f_1 \to \infty$, B_w approaches the limiting value of 2. While the second indicator B_w attaches the importance to the effective frequency bandwidth, the causality ratio R_c emphasizes the optimal trade-off between the low-frequency performance and the actual sample thickness. Based on these two indicators (R_c and B_w), we are able to comprehensively evaluate the overall performance of an absorber.

We summarize in Table 1 the performance of the present absorber and a number of competitive metamaterial absorbers (22, 23, 25, 28) as well as the conventional foam absorber with the same thickness (14.2 mm). The latter comparison is obligated by our use of the foam patches in our sample, with the purpose of showing the foam to be only partially responsible for the success of our absorber. It can be seen that our absorber has a larger B_w and a smaller R_c than all the competitors. For example, while the absorber of ref. 28 has a better absorption performance, its thickness is relatively large, and the operating bandwidth is limited. Also, despite a thin thickness of 3.53 mm for the absorber in ref. 25, the reflection loss is not as competitive as others. It is worth mentioning that the conventional foam is already an effective absorber, especially for higher frequencies (see green triangles in Fig. 3*C*). In fact, other carbon-based materials (51–54) also exhibit similar excellent absorption capabilities at higher frequencies.

Polarization Independence and Oblique Incidence Performance. In a complex electromagnetic environment, the performance of a microwave absorber must be averaged over various oblique incident angles under random polarizations. Hence, it is of great importance to check the absorption performance with different polarizations as well as with oblique incident angles. Because of the symmetry of the designed structure, at normal incidence, the transverse electric field (TE) excitation and transverse magnetic field (TM) excitation are identical and therefore lead to the same reflection loss. Hence, it can be concluded that the absorber is polarization independent at normal incidence (*SI Appendix*, *Polarization independence and oblique incidence performance*).

At oblique incidence, the reflection coefficients are different for the TE and TM polarizations (12). The reflection loss spectra of the two cases are separately displayed in *SI Appendix*, *Polarization independence and oblique incidence performance*. Here, for simplicity, we average the reflection loss with TE and TM polarizations and plot the results in Fig. 4. Both the simulation and experimental results show that under 22.5° oblique incidence (Fig. 4 *A* and *C*), the reflection loss averaged over 3 to 40 GHz is −17.6 dB, comparable with that under normal incidence in Fig. 3*C*, indicating the sample's insensitivity to the incidence angle. For a larger oblique incident angle of 45°, even without the foam, the hierarchical structure can already display efficient performance with over −10 dB reflection loss (Fig. 4*B*). With the assistance of the dissipative foam patches, the reflection loss spectrum is smoothed (Fig. 4*D*) and displays an average reflection loss of −16.3 dB. The dissipation of the foam patches converts the majority of diffraction components into absorption inside the sample. This is evidenced through simulations by a direct calculation of the diffracted energy, presented in *SI Appendix*, *Diffraction orders and their absorption*.

Conclusion and Outlook

We report a microwave absorber design based on the collective (electrical) dipole resonance that, upon interaction with its image through a PEC plane, leads to two high-impedance resonances. With deliberately controlled loss in conjunction with a staggered hierarchical structure, near-perfect absorption is achieved from 3 GHz onward, covering the whole 5G high-frequency bands. The thickness of the hierarchically structured absorber very closely approaches the causality limit as dictated by the reflection spectrum. Despite the excellent performance, the basic building element is a simple metallic ring printed on PCB substrate, which is foreseen to facilitate the future applications with low-cost mass production. In past works, the metamaterial absorbers often work in the subwavelength regime, below a cutoff frequency determined by the lattice constant. Our absorber breaks this limit by introducing self-similar structures attendant with the absorption of the diffracted beams by dissipative foam, thereby extending the absorption capability to a much higher frequency regime. The basic conceptual elements adopted in this work may have potential in

Table 1. The performances of our absorber compared with the microwave-absorbing foam and other selected competitive metamaterial absorbers

Reference	Thickness	Operating band	B_w	Averaged reflection loss (dB)	R_c
Our work	14.2 mm	3 to 40 GHz	1.72	−19.4 dB	1.05
Foam	14.2 mm	3 to 40 GHz	1.72	−15.4 dB	1.40
Ref. 22	10.0 mm	5.2 to 18.0 GHz	1.10	−14.3 dB	N.A.
Ref. 23	13.3 mm	2.1 to 9.1 GHz	1.25	−17.7 dB	1.23
Ref. 25	3.5 mm	6.8 to 19.4 GHz	0.96	−14.0 dB	N.A.
Ref. 28	40.0 mm	1.1 to 2.0 GHz	0.58	−20.9 dB	1.43

The operating bands and the related averaged reflection loss are evaluated from the published experimental results. The displayed values of R_c are from the relevant references. Here, N.A. means not available in cited works.

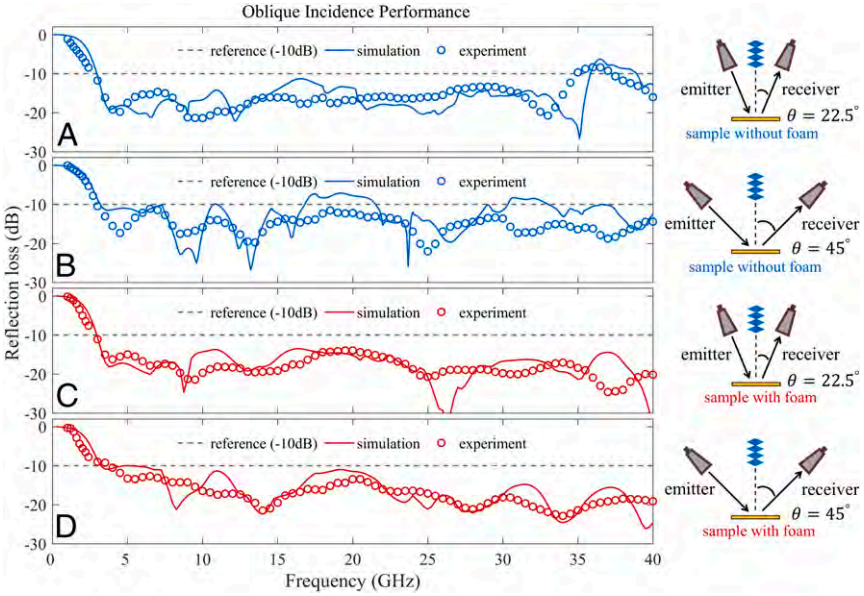

Fig. 4. Oblique incidence performance. (*A* and *B*) The reflection loss of the sample without the foam patches. (*C* and *D*) The reflection loss of the sample with the foam patches. The reflection loss spectra (in dB scale) under oblique incidence are averaged using the data of TE and TM polarizations. The solid lines are the simulation results of the reflection loss, while the open circles denote the measured results. For comparison, *A* and *C* show the results under an oblique incidence angle of 22.5°, while *B* and *D* are corresponding to 45°. The gray dashed lines denote the reference for −10 dB reflection loss.

designing versatile devices with broadband performance, such as tunable waveguides (55–57), electromagnetic cloak (58, 59), metamaterial-based antenna (60), achromatic metalens (61), etc.

Materials and Methods

Sample Fabrication. The PCB technology was adopted to fabricate the sample. All the metallic rings were printed with electro-deposited copper, which is available for high etching accuracy and large circuit density. With the surface-mounted technology, the lumped chip resistors (R0201 or R01005) were soldered on either the larger or the smaller rings. The resistor dimensions were chosen to be small enough to minimize the parasitic effects (6) at higher frequencies. The circuit board was subsequently cut into long strips with equally spaced rectangular slots. The stripes were then assembled into a square checkerboard array for both the larger and smaller metallic rings. Finally, the microwave-absorbing foam (Dalian Dongxin FCT40) was cut into square patches to fill the interstitial spaces of the square larger-ring array. The lateral dimension of the measured sample is 22 × 22 cm.

Far-Field Measurements. The sample performance was measured inside a microwave dark room with the dimensions of 1.5 × 1.5 × 2.5 m. The six inner walls of the dark room were covered by pyramidal-shaped, thick microwave-absorbing foam to create a reflection-free space. We adopted three pairs of double-ridge antennas, which were responsible for the frequency bands 1 to 20 GHz (HZ-10200-DRHA-10), 6 to 18 GHz (MX-0618-DRHA-16), and 18 to 40 GHz (MX-1840-DRHA-16). For a targeted frequency band, one antenna served as an emitter and the other as the receiver. If the characteristic diameter of the antenna is D_h, the distance between the antenna and the sample should satisfy the relation $L_{hs} > 2D_h^2/\lambda$ so as to reach the far-field plane wave radiation condition. The antennas were connected to the vector network analyzer (Keysight N5320B) via the coaxial cables (Lair UF40) whose cutoff frequency is higher than 40 GHz. A flat, 3.2-mm-thick aluminum plate with the same lateral dimensions as the sample was used to calibrate each measurement. We varied the polarizations of the incident microwave by rotating the azimuth of the antenna horn.

Simulation Methods. In numerical simulations, the CST Studio Suite was adopted for fast and efficient computation of the individual layer of the absorber, thanks to the finite-difference time-domain method. The optimization toolbox and parametric-scanning function of CST Studio Suite can be used to find the best parameters. Another commercial software we used is COMSOL Multiphysics (Radio Frequency Module) based on the finite element method. The COMSOL Multiphysics was responsible for the calculation of reflection and diffraction for the hierarchical structure. Both software support the lumped elements used to model the loaded resistors. For the absorption frequency band without diffraction (in the subwavelength region $a_1 < \lambda$), there was no difference whether we used PEC and PMC side boundaries or the Floquet periodic boundary conditions to guide the plane wave with normal incident angle. However, for the case involving diffraction orders and oblique incidence, only the Floquet periodic boundary condition was appropriate, and the diffraction was calculated by using only COMSOL Multiphysics. The mesh size was set to be smaller than 1/6 wavelength in order to ensure accurate outcomes.

Data Availability. All study data are included in the article and/or *SI Appendix*.

ACKNOWLEDGMENTS. P.S. acknowledges the support of the Hong Kong Research Grant Council's Research Impact Fund R6015-18 for this work. S.Q. wishes to thank Min Yang for helpful discussions on the simulations. S.Q., Y.H., and P.S. wish to thank David Mak, Walter Ho, and T.K. Cheung for the help in the dark room setup.

1. A. Al-Dulaimi, S. Al-Rubaye, Q. Ni, E. Sousa, 5G communications race: Pursuit of more capacity triggers LTE in unlicensed band. *IEEE Veh. Technol. Mag.* **10**, 43–51 (2015).
2. R. N. Kostoff, P. Heroux, M. Aschner, A. Tsatsakis, Adverse health effects of 5G mobile networking technology under real-life conditions. *Toxicol. Lett.* **323**, 35–40 (2020).
3. C. L. Russell, 5 G wireless telecommunications expansion: Public health and environmental implications. *Environ. Res.* **165**, 484–495 (2018).
4. M. Simkó, M.-O. Mattsson, 5G wireless communication and health effects – A pragmatic review based on available studies regarding 6 to 100 GHz. *Int. J. Environ. Res. Public Health* **16**, 3406 (2019).
5. H. W. Ott, *Electromagnetic Compatibility Engineering* (John Wiley & Sons, 2011).
6. D. M. Pozar, *Microwave Engineering* (John Wiley & Sons, 2011).
7. A. P. Raman, M. A. Anoma, L. Zhu, E. Rephaeli, S. Fan, Passive radiative cooling below ambient air temperature under direct sunlight. *Nature* **515**, 540–544 (2014).
8. A. Raveendran, M. T. Sebastian, S. Raman, Applications of microwave materials: A review. *J. Electron. Mater.* **48**, 2601–2634 (2019).
9. X. Shen *et al.*, Triple-band terahertz metamaterial absorber: Design, experiment, and physical interpretation. *Appl. Phys. Lett.* **101**, 154102 (2012).
10. H. Tao *et al.*, A metamaterial absorber for the terahertz regime: Design, fabrication and characterization. *Opt. Express* **16**, 7181–7188 (2008).
11. H.-T. Chen *et al.*, Antireflection coating using metamaterials and identification of its mechanism. *Phys. Rev. Lett.* **105**, 073901 (2010).
12. C. T. Riley *et al.*, Near-perfect broadband absorption from hyperbolic metamaterial nanoparticles. *Proc. Natl. Acad. Sci. U.S.A.* **114**, 1264–1268 (2017).

13. X. Liu, T. Starr, A. F. Starr, W. J. Padilla, Infrared spatial and frequency selective metamaterial with near-unity absorbance. *Phys. Rev. Lett.* **104**, 207403 (2010).
14. X. Liu *et al*., Taming the blackbody with infrared metamaterials as selective thermal emitters. *Phys. Rev. Lett.* **107**, 045901 (2011).
15. K. Aydin, V. E. Ferry, R. M. Briggs, H. A. Atwater, Broadband polarization-independent resonant light absorption using ultrathin plasmonic super absorbers. *Nat. Commun.* **2**, 517 (2011).
16. Y. Huang *et al*., A refractory metamaterial absorber for ultra-broadband, omnidirectional and polarization-independent absorption in the UV-NIR spectrum. *Nanoscale* **10**, 8298–8303 (2018).
17. N. I. Landy, S. Sajuyigbe, J. J. Mock, D. R. Smith, W. J. Padilla, Perfect metamaterial absorber. *Phys. Rev. Lett.* **100**, 207402 (2008).
18. V. S. Asadchy *et al*., Broadband reflectionless metasheets: Frequency-selective transmission and perfect absorption. *Phys. Rev. X* **5**, 031005 (2015).
19. D. Ye *et al*., Towards experimental perfectly-matched layers with ultra-thin metamaterial surfaces. *IEEE Trans. Antenn. Propag.* **60**, 5164–5172 (2012).
20. Q.-Y. Wen, H.-W. Zhang, Y.-S. Xie, Q.-H. Yang, Y.-L. Liu, Dual band terahertz metamaterial absorber: Design, fabrication, and characterization. *Appl. Phys. Lett.* **95**, 241111 (2009).
21. X. Li *et al*., Dispersion engineering in metamaterials and metasurfaces. *J. Phys. D Appl. Phys.* **51**, 054002 (2018).
22. J. Zhao, Y. Cheng, Ultrabroadband microwave metamaterial absorber based on electric SRR loaded with lumped resistors. *J. Electron. Mater.* **45**, 5033–5039 (2016).
23. Y. Shang, Z. Shen, S. Xiao, On the design of single-layer circuit analog absorber using double-square-loop array. *IEEE Trans. Antenn. Propag.* **61**, 6022–6029 (2013).
24. A. Kazemzadeh, Nonmagnetic ultrawideband absorber with optimal thickness. *IEEE Trans. Antenn. Propag.* **59**, 135–140 (2010).
25. J. Zhao, C. Zhang, Q. Cheng, J. Yang, T. J. Cui, An optically transparent metasurface for broadband microwave antireflection. *Appl. Phys. Lett.* **112**, 073504 (2018).
26. Y. Shen *et al*., An extremely wideband and lightweight metamaterial absorber. *J. Appl. Phys.* **117**, 224503 (2015).
27. F. Ding, Y. Cui, X. Ge, Y. Jin, S. He, Ultra-broadband microwave metamaterial absorber. *Appl. Phys. Lett.* **100**, 103506 (2012).
28. D. Ye *et al*., Ultrawideband dispersion control of a metamaterial surface for perfectly-matched-layer-like absorption. *Phys. Rev. Lett.* **111**, 187402 (2013).
29. Y. Cui *et al*., Ultrabroadband light absorption by a sawtooth anisotropic metamaterial slab. *Nano Lett.* **12**, 1443–1447 (2012).
30. H. Xiong, J.-S. Hong, C.-M. Luo, L.-L. Zhong, An ultrathin and broadband metamaterial absorber using multi-layer structures. *J. Appl. Phys.* **114**, 064109 (2013).
31. W.-L. Song *et al*., Constructing repairable meta-structures of ultra-broad-band electromagnetic absorption from three-dimensional printed patterned shells. *ACS Appl. Mater. Interfaces* **9**, 43179–43187 (2017).
32. Y. Wang *et al*., 5G mobile: Spectrum broadening to higher-frequency bands to support high data rates. *IEEE Veh. Technol. Mag.* **9**, 39–46 (2014).
33. K. N. Rozanov, Ultimate thickness to bandwidth ratio of radar absorbers. *IEEE Trans. Antenn. Propag.* **48**, 1230–1234 (2000).
34. S. Qu, P. Sheng, Minimizing indoor sound energy with tunable metamaterial surfaces. *Phys. Rev. Appl.* **14**, 034060 (2020).
35. M. Xie, M. Yang, S. Xiao, Y. Xu, S. Chen, Acoustic metal. arXiv [Preprint] (2020). https://arxiv.org/abs/2010.02813v1 (Accessed 27 May 2021).
36. M. Yang, S. Chen, C. Fu, P. Sheng, Optimal sound-absorbing structures. *Mater. Horiz.* **4**, 673–680 (2017).
37. M. Yang, P. Sheng, Sound absorption structures: From porous media to acoustic metamaterials. *Annu. Rev. Mater. Res.* **47**, 83–114 (2017).
38. M. Yang, P. Sheng, An integration strategy for acoustic metamaterials to achieve absorption by design. *Appl. Sci. (Basel)* **8**, 1247 (2018).
39. R. M. Fano, Theoretical limitations on the broadband matching of arbitrary impedances. *J. Franklin Inst.* **249**, 57–83 (1950).
40. A. Shlivinski, Y. Hadad, Beyond the bode-fano bound: Wideband impedance matching for short pulses using temporal switching of transmission-line parameters. *Phys. Rev. Lett.* **121**, 204301 (2018).
41. Y. Ra'Di, C. Simovski, S. Tretyakov, Thin perfect absorbers for electromagnetic waves: Theory, design, and realizations. *Phys. Rev. Appl.* **3**, 037001 (2015).
42. Y. P. Lee, J. Y. Rhee, Y. J. Yoo, K. W. Kim, "Broadband and Tunable MMPA" in *Metamaterials for Perfect Absorption* (Springer, 2016), pp. 113–141.
43. J. D. Jackson, *Classical Electrodynamics* (American Association of Physics Teachers, 1999).
44. D. R. Smith, J. B. Pendry, M. C. Wiltshire, Metamaterials and negative refractive index. *Science* **305**, 788–792 (2004).
45. J. B. Pendry, A. J. Holden, D. J. Robbins, W. Stewart, Magnetism from conductors and enhanced nonlinear phenomena. *IEEE Trans. Microw. Theory Tech.* **47**, 2075–2084 (1999).
46. T.-J. Yen *et al*., Terahertz magnetic response from artificial materials. *Science* **303**, 1494–1496 (2004).
47. G. Ma, M. Yang, S. Xiao, Z. Yang, P. Sheng, Acoustic metasurface with hybrid resonances. *Nat. Mater.* **13**, 873–878 (2014).
48. S. T. Tang, X. Zhang, C. Meng, Z. Yang, Pressure monopoles, velocity monopoles, and hybrid monopoles in acoustics. *Phys. Rev. Appl.* **11**, 014008 (2019).
49. M. Yang *et al*., Subwavelength total acoustic absorption with degenerate resonators. *Appl. Phys. Lett.* **107**, 104104 (2015).
50. X. Chen, T. M. Grzegorczyk, B.-I. Wu, J. Pacheco Jr, J. A. Kong, Robust method to retrieve the constitutive effective parameters of metamaterials. *Phys. Rev. E Stat. Nonlin. Soft Matter Phys.* **70**, 016608 (2004).
51. L. Kong *et al*., Recent progress in some composite materials and structures for specific electromagnetic applications. *Int. Mater. Rev.* **58**, 203–259 (2013).
52. K.-L. Zhang, J.-Y. Zhang, Z.-L. Hou, S. Bi, Q.-L. Zhao, Multifunctional broadband microwave absorption of flexible graphene composites. *Carbon* **141**, 608–617 (2019).
53. Y. Huang *et al*., Multi-scale design of electromagnetic composite metamaterials for broadband microwave absorption. *Compos. Sci. Technol.* **162**, 206–214 (2018).
54. J. Ning *et al*., Ultra-broadband microwave absorption by ultra-thin metamaterial with stepped structure induced multi-resonances. *Results Phys.* **18**, 103320 (2020).
55. N. Gao, J. Li, R. H. Bao, W. Q. Chen, Harnessing uniaxial tension to tune Poisson's ratio and wave propagation in soft porous phononic crystals: An experimental study. *Soft Matter* **15**, 2921–2927 (2019).
56. Y. Long *et al*., Designing all-electric subwavelength metasources for near-field photonic routings. *Phys. Rev. Lett.* **125**, 157401 (2020).
57. N. Gao, S. Qu, L. Si, J. Wang, W. Chen, Broadband topological valley transport of elastic wave in reconfigurable phononic crystal plate. *Appl. Phys. Lett.* **118**, 063502 (2021).
58. S. Xu *et al*., Broadband surface-wave transformation cloak. *Proc. Natl. Acad. Sci. U.S.A.* **112**, 7635–7638 (2015).
59. D. Schurig *et al*., Metamaterial electromagnetic cloak at microwave frequencies. *Science* **314**, 977–980 (2006).
60. E. Lier, D. H. Werner, C. P. Scarborough, Q. Wu, J. A. Bossard, An octave-bandwidth negligible-loss radiofrequency metamaterial. *Nat. Mater.* **10**, 216–222 (2011).
61. S. Wang *et al*., A broadband achromatic metalens in the visible. *Nat. Nanotechnol.* **13**, 227–232 (2018).

PNAS
www.pnas.org

Supplementary Information for

Conceptual-based design of ultrabroadband microwave metamaterial absorber

Sichao Qu, Yuxiao Hou, Ping Sheng*

Department of Physics, The Hong Kong University of Science and Technology

Clear Water Bay, Kowloon, Hong Kong, China

*Email: sheng@ust.hk

This PDF file includes:

Contents

Supporting Text 1. Sample geometry

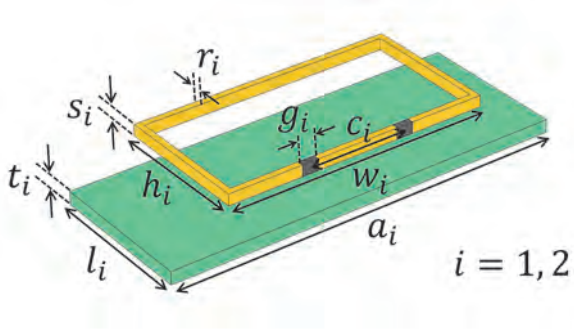

Fig. S1 The geometric parameters for the ring structure, with the (green) PCB substrate. The subscript $i = 1, 2$ denotes the particular length for the larger or smaller ring-structure. The grey patches denote the two resistors.

For the structure of the larger-ring unit, the dimensions are $l_1 = 9.1$ mm, $h_1 = 8.3$ mm, $w_1 = 16$ mm and $a_1 = 24$ mm [see Fig. S1]. In the initial simulations, the large ring is placed in the centre of the PCB substrate. However, after introducing the PEC plane, the upper side of the larger ring-structure is set to be tangential to the upper edge of the FR-4 substrate, whose thickness is $t_1 = 0.77$ mm. The distance between the centres of the two lumped resistors is $c_1 = 6$ mm. The thickness (along the out-of-plane direction) of the larger ring is $s_1 = 0.685$ mm. The width of metallic line is $r_1 = 0.38$ mm. The split gap for the resistors is $g_1 = 1$ mm, which is much smaller than the relevant wavelength. For the similar structure of the smaller-ring unit, the dimensions are: $l_2 = 5.1$ mm, $h_2 = 2.7$ mm, $w_2 = 4.7$ mm, $a_2 = 6$ mm, $t_2 = 0.127$ mm, $s_1 = 0.035$ mm, $r_2 = 0.28$ mm, and $g_2 = 0.2$ mm. In addition, the smaller ring is placed in

the centre of the Rogers-5880 substrate. The overall thickness of the integrated hierarchical structure is $l_1 + l_2 = 14.2$ mm. The geometric parameters mentioned above were used in both simulation modelling and sample fabrication.

Supporting Text 2. Extraction method for the effective parameters

In this section, the relation between the effective electric and magnetic parameters and S-parameters is derived. Here we treat the absorbing-layer as a homogeneous medium characterized by the effective permittivity ϵ_{eff} and permeability μ_{eff}. Consider a plane wave coming from one side, passing through the absorbing layer and then onto the semi-infinite space. In the time-stationary state, the total fields can be decomposed according to the two opposite directions of the wave vectors. Hence the incident, reflected and transmitted electric and magnetic fields can be written as

$$\begin{cases} \boldsymbol{E}_i = E_i \exp\left[i(kz-\omega t)\right]\boldsymbol{e}_y,\ \boldsymbol{H}_i = E_i \exp\left[i(kz-\omega t)\right]\boldsymbol{e}_x / Z_0, \\ \boldsymbol{E}_r = E_r \exp\left[i(-kz-\omega t)\right]\boldsymbol{e}_y,\ \boldsymbol{H}_r = -E_r \exp\left[i(-kz-\omega t)\right]\boldsymbol{e}_x / Z_0, \\ \boldsymbol{E}_t = E_t \exp\left[i(kz-\omega t)\right]\boldsymbol{e}_y,\ \boldsymbol{H}_t = E_t \exp\left[i(kz-\omega t)\right]\boldsymbol{e}_x / Z_0, \end{cases} \tag{S1}$$

where Z_0 is the vacuum impedance and k is the amplitude of the wave vector. In the absorbing layer, the electric and magnetic fields are given by

$$\begin{cases} \boldsymbol{E}_i' = E_i' \exp\left[i(k'z-\omega t)\right]\boldsymbol{e}_y,\ \boldsymbol{H}_i' = E_i' \exp\left[i(k'z-\omega t)\right]\boldsymbol{e}_x / Z_{\text{eff}}, \\ \boldsymbol{E}_r' = E_r' \exp\left[i(-k'z-\omega t)\right]\boldsymbol{e}_y,\ \boldsymbol{H}_r' = -E_r' \exp\left[i(-k'z-\omega t)\right]\boldsymbol{e}_x / Z_{\text{eff}}, \end{cases} \tag{S2}$$

where $k' = n_{\text{eff}}k$. Here n_{eff}, Z_{eff} are the effective refraction index and impedance, respectively. In order to simplify the upcoming equations, we define $X = \exp(ik'd)$, $z_{\text{r}} = Z_{\text{eff}}/Z_0$, $S_{11} = E_r/E_i$, $S_{21} = E_t\exp(ikd)/E_i$, $\alpha = E_i'/E_i$ and $\beta = E_r'/E_i$. Here $Z_{\text{eff}} = \sqrt{\mu_{\text{eff}}/\epsilon_{\text{eff}}}$ and $n_{\text{r}} = \sqrt{\epsilon_{\text{r}}\mu_{\text{r}}}$, where $\epsilon_r = \epsilon_{\text{eff}}/\epsilon_0$ and $\mu_r = \mu_{\text{eff}}/\mu_0$. By using the above notation convention, the boundary conditions for electric fields at the two interfaces can be simplified as:

$$at\ z=0:\ \begin{cases} 1+S_{11} = \alpha+\beta \\ 1-S_{11} = (\alpha-\beta)/z_r \end{cases},\qquad at\ z=d:\ \begin{cases} \alpha X + \beta X^{-1} = S_{21} \\ (\alpha X - \beta X^{-1})/z_r = S_{21} \end{cases}. \tag{S3}$$

By cancelling α and β, we obtain the relations

$$\begin{aligned} \frac{Z_{\text{eff}}}{Z_0} = z_r &= \pm\sqrt{\frac{(1+S_{11})^2 - S_{21}^2}{(1-S_{11})^2 - S_{21}^2}}, \\ X = \exp(in_r kd) &= \frac{S_{21}}{1 - S_{11}(z_r-1)/(z_r+1)}. \end{aligned} \tag{S4}$$

Hence, the effective normalized impedance and refraction index can be retrieved from the S-parameters. For a passive medium, the uncertainty in the sign of z_r is eliminated by the condition $\text{Re}(z_r) > 0$ and the ambiguity of the branch of n_r (because of the logarithm function) can be determined by the method used in Ref. (1). In addition, the effective permittivity ϵ_{eff} and permeability μ_{eff} are given by $\epsilon_{\text{eff}} = (n_r/z_r)\epsilon_0$, $\mu_{\text{eff}} = (n_r z_r)\mu_0$. The extraction method above

was used to engineer the dispersion of the metamaterial absorber in the main text. Because our absorber was backed by the perfect electric conductor boundary (PEC), in simulations four small holes were opened at the corners of PEC, in order to allow small transmission as a perturbation (2). Although the transmission is negligible, its phase information is indispensable for the extraction method.

Supporting Text 3. Theoretical requirements for near-perfect absorption

Based on the effective medium description, one can find out what theoretical requirements should be satisfied by the effective parameters for an electromagnetic absorber to achieve near-perfect absorption. Since the absorption coefficient is given by $A = 1 - |S_{11}|^2 - |S_{21}|^2$, high absorption means minimizing $|S_{11}|$ and $|S_{21}|$. The small value of $|S_{21}|$ has been guaranteed by the PEC backing. Hence, if we want to $S_{11} \to 0$ and $S_{21} \to 0$, Eq.(S4) yields the well-known impedance matching condition (i.e., $z_r = 1$ or $n_r = \sqrt{\epsilon_r \mu_r} = \epsilon_r = \mu_r$), just as expected. Meanwhile, Eq. (S4) forces the variable $X = \exp(n_r kd) = \exp(i\,\mathrm{Re}[\epsilon_r] kd)\exp(-\mathrm{Im}[\epsilon_r] kd) \to 0$. Therefore, in order to achieve near-perfect absorption, the following requirements should be satisfied:

$$\begin{cases} \epsilon_r / \mu_r = 1, \\ \mathrm{Im}(\epsilon_r) kd = \mathrm{Im}(\mu_r) kd \gg 1. \end{cases} \tag{S5}$$

The first one is the impedance-matching condition, for minimizing the reflection from the surface of the absorber. The second one means that the dissipation inside the absorber should be large enough to attenuate the energy of the waves. Also, the same absorption performance at a higher frequency can be achieved by either a thinner thickness or smaller imaginary parts, since the wave vector is proportional to the frequency. This inference is consistent with the fact that the lower-frequency absorption is more difficult. It should be noted that Eq. (S5) cannot be strictly satisfied at all frequencies, owing to the inherent constraint set by the Kramer-Kronig relation (3) that links the real and imaginary parts of the effective permittivity $\epsilon_{\mathrm{eff}}(\omega)$ and permeability $\mu_{\mathrm{eff}}(\omega)$ over the whole frequency range. Our dispersion engineering has the goal of maximizing the frequency spectrum over which Eq.(S5) can be optimally satisfied.

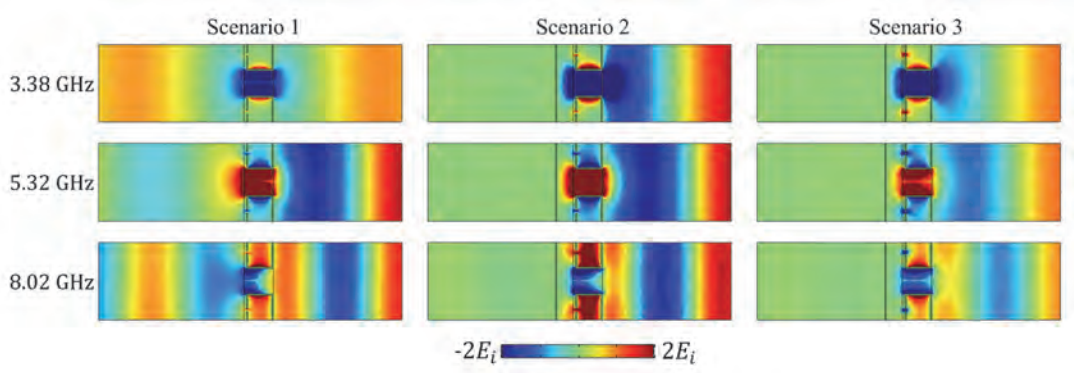

Fig. S2 The electric field distribution in three different scenarios at 3.38 GHz, 5.32 GHz, and 8.02 GHz. Scenario 2 is the same one discussed in main text, corresponding to the electric and magnetic resonances. The black line to the left of the ring in scenarios 2 and 3 represents the PEC backing. The green region means there is no electric field. Here the incident wave is from the right side.

Supporting Text 4. Comparison of the dipole modes under three scenarios

In order to enhance our understanding of the structural resonances of the ring, we divide the simulations into three different scenarios (Scenario 1: without the PEC backing; Scenario 2: with PEC backing; Scenario 3: with PEC backing and optimally-tuned resistors). In Fig. S2, we plot the electric fields on the cutting planes parallel to the ring's plane. The resistance was set to be close to zero in the simulations of scenarios 1 and 2. For each frequency, the dipole modes on the ring were excited by the incident wave coming from the right side, giving rise to very similar patterns around the capacitive gap. Thus, the lossy dipole resonance on the metallic ring may be excited over a broad frequency band. By comparing scenario 1 with scenario 2, the only difference is that with the presence of the PEC backing, the transmitted wave is reflected by PEC to form a longitudinal standing wave in scenario 2 (thus the electric and magnetic resonances or PEC and PMC effects). Moreover, by comparing scenario 2 with scenario 3 (i.e., impedance matching), we can see that the amplitude of the electric field is approximately $2E_i$ and E_i, respectively, which is reasonable.

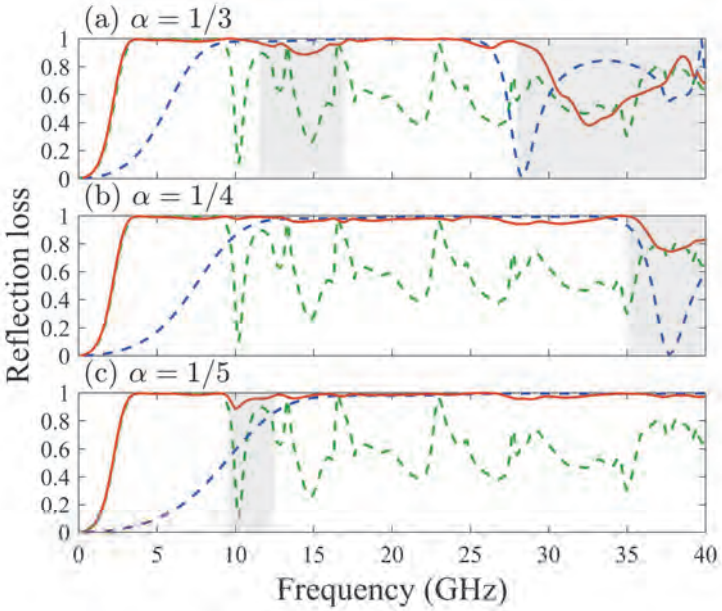

Fig. S3 Reflection loss spectra with different scaling factor values. (a) $\alpha = 1/3$, (b) $\alpha = 1/4$, (c) $\alpha = 1/5$. The green and blue dashed line denote the absorption of the individual larger and smaller ring-structures, respectively. The orange line denotes the performance of the integrated hierarchical structure. The grey-shaded regions are meant to indicate the frequency ranges with relatively poor performance. It is seen that with $\alpha = 1/4$, only a small high frequency regime is poor; however, that range can be easily compensated by the use of foam patches.

Supporting Text 5. Scaling factor determination

We determine the scaling factor α by trying different values [see Fig. S3] and identifying the optimal value by using simulation. It is found that if $\alpha = 1/3$, the smaller ring-structure is relatively too large and the coupling between the two layers is strong, which can lead to imperfect splicing of the two spectra. If $\alpha = 1/5$, the starting absorbing frequency is too high, which can cause a dip in the spliced spectrum around 10 GHz. Therefore, by considering the simulation results comprehensively, we choose $\alpha = 1/4$ as the best value that can combine the two individual absorption spectra.

In spite of the drop of the reflection loss above 35 GHz for $\alpha = 1/4$, that part can be fixed by integrating our metamaterial sample with foam patches. We choose the denominator to be an integer, in order to let the unit cell to be well-defined.

Supporting Text 6. Modelling the foam by using the Debye model

The conventional microwave absorbing foam is a porous material, dispersed with carbon-based particles. Its normalized effective permeability should be treated as $\mu_r \cong 1$ and its normalized effective permittivity is function of frequency, $\epsilon_r(\omega)$. In order to correctly capture the causal nature of $\epsilon_r(\omega)$, we adopt the Debye model (4) with multiple relaxation regimes to mimick its wideband lossy feature. According to the Debye model, the normalized effective permittivity can be written as

$$\epsilon_{\mathrm{r}}(\omega) = \epsilon_{\infty} + \sum_{i=1}^{N} \frac{\Delta\epsilon_i}{1 - i\omega\tau_i}, \tag{S6}$$

where $\epsilon_{\infty} = 1$, τ_i is the relaxation time of the i_{th} relaxation process and N is the total number of relaxation regimes. By defining $x_i = 10^{-\tau_i}$ that is continuously and evenly distributed in the range of (m_l, m_u), we can simplify Eq.(S6) to the following form:

$$\epsilon_{\mathrm{r}}(\omega) = \epsilon_{\infty} + \frac{\Delta\epsilon}{m_u - m_l}\int_{m_l}^{m_u} \frac{dx}{1 - i\omega/10^{x}} = \epsilon_{\infty} + \frac{\Delta\epsilon}{m_u - m_l}\log_{10}\left(\frac{\tau_l - i\omega\tau_l\tau_u}{\tau_u - i\omega\tau_l\tau_u}\right). \tag{S7}$$

We characterize the foam by adjusting the parameters to fit the experimental data. The outcomes are $\Delta\epsilon = 0.8, m_l = 11.10, m_u = 11.42, \tau_l = 7.96 \times 10^{-12}\mathrm{s}, \tau_u = 3.7894 \times 10^{-12}\mathrm{s}$. By adopting these values, the real part of ϵ_r is found to be slightly greater than unity and the imaginary part is 0.1~0.2 within the relevant frequency regime of our work. We use this model throughout the simulations involving diffraction in the high-frequency regime.

Supporting Text 7. Diffraction orders and their absorption

Beyond 12.5 GHz, the hierarchical structure can be treated as a reflecting two-dimensional tetragonal grating, with a lattice constant of $a_1 = 24$ mm. The length of the lattice vector can be written as $G_1 = G_2 = 2\pi/a_1$. Consider an oblique incident wave with wave vector $\boldsymbol{k}$, which can be decomposed into

$$\boldsymbol{k} = \boldsymbol{k}_{\parallel} + \boldsymbol{k}_{\perp}, \tag{S8}$$

where $k = \omega/c_0$, $\boldsymbol{k}_{\parallel}$ is the in-plane wave vector and $\boldsymbol{k}_{\perp}$ is the out-of-plane wave vector. In this notation, the incident angle is given by $\theta = \arctan(k_{\parallel}/k_{\perp})$. As an example, in Fig. S4, we show the case with an oblique incident angle of 24.6° at 15 GHz. The essence of diffraction is to recognize that (a) the momentum of the lattice is transferred to the incident wave, and (b) the discretized momenta that the lattice is allowed to transfer is determined by the reciprocal lattice vectors (3). In Fig. S4, only the diffraction orders within the circle with its radius dictated by k, are propagating modes [see the four diffraction propagating orders in Fig. S4(a)]. Outside the circle, the diffraction orders are non-

propagating evanescent waves. However, if the frequency increases, there can be more and more emerging diffracted orders. For another example, with a 40 GHz normal incident wave, our sample allows the diffraction orders (m, n) with the condition:

$$\sqrt{(mG_1)^2 + (nG_2)^2} < k, \tag{S9}$$

which can be simplified as $\sqrt{m^2 + n^2} < 3.2$. After some simple calculation, we can predict that there can be scattering waves with 7 different diffraction angles, with a total diffraction-order number of 36. Because each diffraction order can be decomposed into TE and TM polarizations, there are actually 72 types of diffracted waves. We have double-checked our diffraction simulations by using the RF module of COMSOL Multiphysics and obtained consistent results.

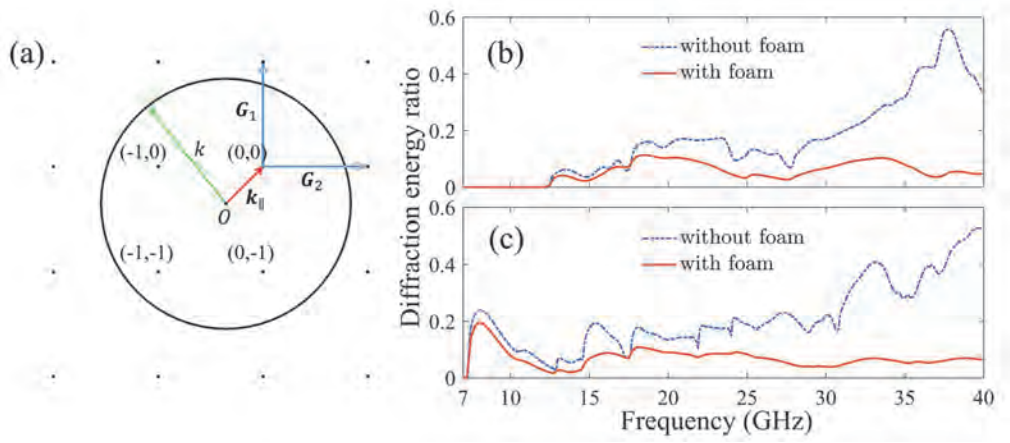

Fig. S4 (a) The diffraction orders in the reciprocal lattice, showing the reciprocal lattice vectors G_1 and G_2, the in-plane wave vector component $k_{\parallel}$, and the circle with a radius k (the incident wave number) enclosing the propagating mode points. (b) For normal incidence, the energy ratios of diffraction D emergent from the sample (without foam and with foam) are plotted as a function of frequency. (c) The same curves for oblique 45° incidence. The results in (c) are that averaged over both the TE and TM incidence. It is seen that the amount of D that emerges from the sample is small after the foam patches are introduced, implying that most of the diffracted energy is absorbed inside the sample.

The diffracted energy comprises contributions from all the diffraction orders, which can be calculated by $D = \sum_{i=2}^{N} |S_{i1}|^2$. The diffraction effect is unavoidable because at higher frequencies, the wavelength is smaller than lateral period of the larger ring-structure. In order to absorb these diffracted orders, we use microwave-absorbing foam to fill the interstitial spaces of the metamaterials (only for the larger ring array). In this way, the diffracted energy can be effectively reduced and turned into the absorbed energy inside the structure. This is seen in Fig. S4(b) and Fig. S4(c) for normal incidence and 45° oblique incidence, respectively, where the dashed line is for the case without the foam patches, and the red solid line is for the case with the inserted foam patches. In the lower frequency range, the diffraction order begins to appear and the diffraction angle (measured from the surface normal) is fairly large, causing the decay length inside the absorber to be relatively large. At higher frequencies, the foam can absorb very efficiently, which explains why the 35-40 GHz reflection loss is improved after using the foam patches. We note that even if a small part

of the large-angle diffracted wave energy escapes the sample, it cannot be detected by horn antenna and have a large probability to be absorbed by the surrounding environment after multiple scatterings.

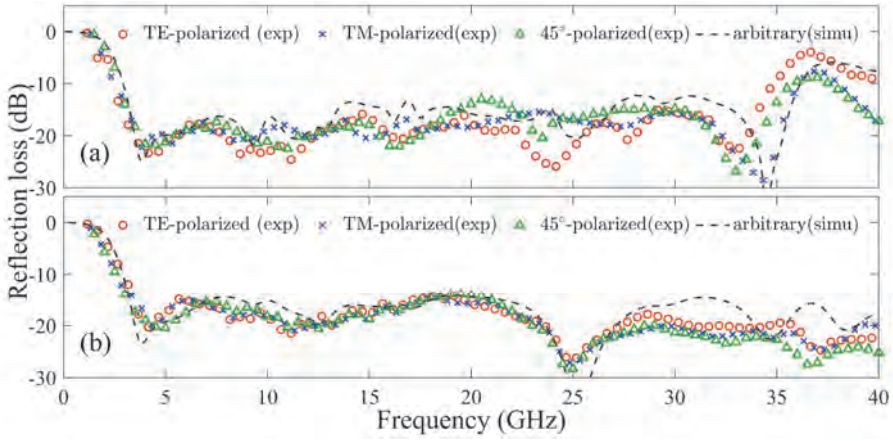

Fig. S5 The reflection loss in dB scale plotted as a function of frequency, when the hierarchical structure is (a) without the foam patches or (b) with the foam patches. The dashed grey lines denote the simulation results, in which the Debye model of a continuous distribution of relaxation times was used to model the foam behavior.

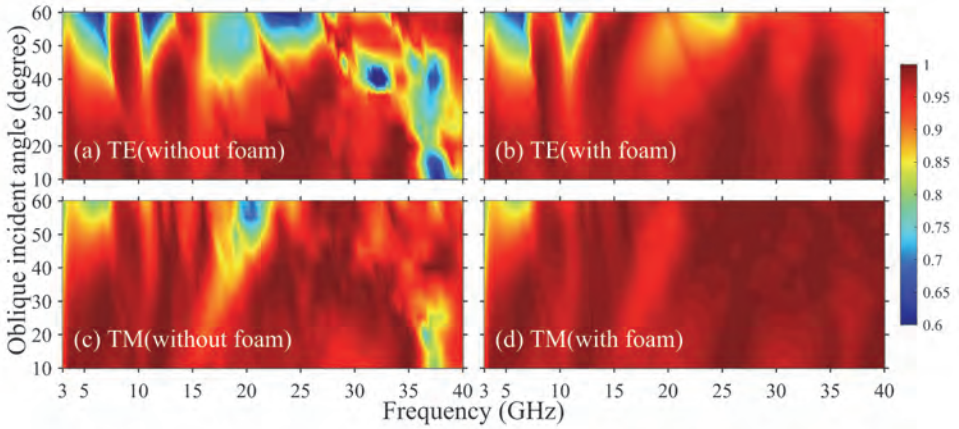

Fig. S6 The simulated reflection loss spectra in linear scale are plotted as a function of the oblique incident angle and the frequency. (a) TE polarization without the foam, (b) TE polarization with the foam, (c) TM polarization without the foam, (d) TM polarization with the foam.

Supporting Text 8. Polarization independence and oblique incidence performance

The geometry of the absorber is designed for the polarization-independent performance at normal incidence. Simulation confirms this point (i.e., arbitrary polarized incident wave gives the same curve). The measured reflection performance is also insensitive to the polarization, no matter the structure is with or without the foam patches [see Fig. S5(a) and Fig. S5(b)]. In the main text, the oblique incidence performances are presented at discretized incident angles and the results are averaged over the TE and TM polarizations. Here, we show the results of TE and TM polarizations separately, and with more incident angles (continuously from 10° to 60°). These are shown in Fig. S6. To sum up briefly, TM polarization incidence can yield better results than the TE polarization; and if the sample is applied with the foam

patches, the higher-frequency and larger-angle performance is greatly enhanced. In practical situations, if we consider the incident wave's polarization angle is random with equal probability, the overall reflection loss can be approximated as the averaged one of TE and TM polarizations, with 50% each. It is seen that the foam can enhance the larger-angle incidence performance.

SI References

1. Chen X, Grzegorczyk TM, Wu B-I, Pacheco Jr J, & Kong JA (2004) Robust method to retrieve the constitutive effective parameters of metamaterials. *Physical Review E* 70(1):016608.
2. Ye D*, et al.* (2012) Towards experimental perfectly-matched layers with ultra-thin metamaterial surfaces. *IEEE Transactions on Antennas and Propagation* 60(11):5164-5172.
3. Jackson JD (1999) *Classical electrodynamics* (American Association of Physics Teachers).
4. Djordjevic AR, Biljié RM, Likar-Smiljanic VD, & Sarkar TK (2001) Wideband frequency-domain characterization of FR-4 and time-domain causality. *IEEE Transactions on Electromagnetic Compatibility* 43(4):662-667.